Supplementary figure legends

Supplementary Fig.1: Loss of *Irf8* recapitulates a chronic-phase CML-like phenotype with inflammatory niche remodeling

(A) Peripheral blood counts of *Irf8*$^{+/+}$, *Irf8*$^{+/d}$ and *Irf8*$^{d/d}$ mice. **(B)** Frequencies of circulating immune cell subsets in peripheral blood, determined by flow cytometry. **(C, D)** Frequencies of immune cells in bone marrow **(C)** and spleen **(D),** determined by flow cytometry. **(E, F)** Frequencies of erythroid lineage cells in bone marrow **(E)** and spleen **(F)**, determined by flow cytometry. **(G, H)** Frequencies of hematopoietic stem and progenitor cells in the bone marrow **(G)** and spleen **(H)**, determined by flow cytometry. **(I)** Quantification of spleen weight, demonstrating significant splenomegaly in *Irf8*$^{d/d}$ mice compared with *Irf8*$^{+/+}$ and *Irf8*$^{+/d}$ mice. **(J)** Representative nearest-neighbor analysis plots of megakaryocytes in bone marrow and spleen. 200 µm = 395 pixels. **(K,L)** Quantification of nearest-neighbour megakaryocyte inter-cell distance **(K)** and megakaryocyte number per cluster **(L)** in bone marrow and spleen, confirming increased megakaryocyte density and clustering in *Irf8*$^{d/d}$ mice normalised to tissue area. **(M)** Immunofluorescence staining of collagen fibers (yellow), Sca-1^{+} stromal cells (turquoise), Endomucin^{+} vessels (pink) in bone marrow of *Irf8*$^{+/+}$ (left) and *Irf8*$^{d/d}$ (right) mice. Scale bar: 20 µm.

Supplementary Fig. 2: *Irf8* deficiency drives compartment-specific stromal remodeling in bone marrow and spleen.

(A) Flow cytometric analysis of CD45^{-} mesenchymal and endothelial populations among viable, lineage-negative cells in the bone marrow of *Irf8*$^{+/+}$ and *Irf8*$^{d/d}$ mice. **(B)** Flow cytometric analysis of CD45^{-} stromal cell subsets among viable, lineage-negative cells in the spleen of *Irf8*$^{+/+}$ and *Irf8*$^{d/d}$ mice.

Supplementary Fig. 3: *Irf8* deficiency couples inflammatory granulopoesis to pro-fibrotic CAR cell remodeling

(A) Dot plot of canonical marker genes supporting cluster annotation of hematopoietic and stromal populations in the dataset. **(B)** Quality control metrics across clusters, illustrating the correlation between totalRNA counts (nCount RNA), number of detected genes (nFeature RNA) and cluster identity. **(C)** Genotype contribution (normalised to total cell number) of *Irf8*$^{+/+}$ and *Irf8*$^{d/d}$ cells across clusters. **(D)** Cell-cycle phase distribution (normalised to total cell number) across clusters. **(E)** Individual pseudotime trajectories for monocytic, erythroid and granulocytic differentiation, reconstructed from hematopoietic progenitors. **(F)** Absolute number of significantly up- or downregulated transcription factors per annotated cell population. **(G)** Volcano plot of selected, differentially expressed genes underlying TNFα pathway activity in mature neutrophils (n = 5,926 total genes) comparing *Irf8*$^{d/d}$ vs. *Irf8*$^{+/+}$ bone marrow. **(H)** Volcano plot of selected, differentially expressed genes underlying TGF-β pathway activity in CAR cells 1 (n = 11,319 total genes) comparing *Irf8*$^{d/d}$ vs. *Irf8*$^{+/+}$ bone marrow. **(I)** Global cell-cell communication heatmap (CrossTalkR) depicting inferred interaction strength between cell populations. **(J)** Frequency of ligand and receptor usage across genotypes. **(K)** Inferred TGF-β-mediated signaling interactions. **(L)** Inferred Itgb1-dependent signaling interactions. **(M)** Hallmark pathway enrichment analysis across cell populations.

Supplementary Fig. 4: Hematopoietic *Irf8* loss is sufficient to activate inflammatory perivascular niche remodeling.

(A) Body weight over time of *Irf8*$^{+/+}$ and *Irf8*$^{d/d}$→Gli1CreERT;tdTomato chimeras, illustrating a chronic, non-aggressive course with stable body weight over 14 weeks. **(B)** Peripheral blood counts. **(C)** Frequencies of peripheral blood immune cell populations determined by flow cytometry. **(D)** Frequencies of bone marrow immune cell populations determined by flow cytometry. **(E, F)** Frequencies of the hematopoietic stem and progenitor cells in the bone marrow **(E)** and spleen **(F). (G)** H&E-stained spleen sections with quantification of white pulp area, revealing reduced white pulp regions in *Irf8*$^{d/d}$→Gli1CreERT;tdTomato chimeras; white pulp regions are highlighted by dashed lines. Scale bar: 300 µm. **(H)** Reticulin staining of spleen and bone marrow sections. Scale bar bone: 60 µm. Scale bar spleen: 300 µm. **(I)** Dot plots of canonical marker genes supporting cluster annotation of hematopoietic and stromal populations. **(J)** Quality control metrics across clusters, illustrating the correlation between total RNA counts (nCount RNA), number of detected genes (nFeature RNA) and cluster identity. **(K)** Cell-cycle phase distribution (normalised to total cell number) across clusters. **(L)** scProportion test assessing genotype contribution of *Irf8*$^{d/d}$ vs. *Irf8*$^{+/+}$ cells across clusters. **(M)** Differentially expressed gene analysis between *Irf8*$^{d/d}$ and *Irf8*$^{+/+}$ bone marrow (FDR = 0.05, $|\log_2 FC| > 0.25$).

Supplementary Fig. 5: Early neutrophil progenitors drive inflammatory and structural remodeling of the vascular niche upon hematopoietic *Irf8* deficiency.
Single-cell transcriptomic analysis of bone marrow from recipient mice reconstituted with *Irf8*$^{+/+}$ or *Irf8*$^{d/d}$ c-Kit-enriched hematopoietic cells.
(A) Global cell-cell communication heatmap (CrossTalkR) depicting inferred interaction strength between cell populations. **(B)** Absolute receptor usage for *S100a8* as a ligand. **(C)** Sankey plot depicting inferred receptor-ligand interactions with a focus on *Tlr4* as a central receptor on arteriolar and sinusoidal endothelial cells. **(D)** Heatmap of blood vessel morphogenesis and angiogenesis-related pathways across selected cell populations, comparing *Irf8*$^{d/d}$ vs. *Irf8*$^{+/+}$ chimeras across clusters. **(E)** Hypoxia (turquoise, HIF-1α)-associated S100A8/9 (white) expression and pro-fibrotic signaling (orange, TGF-β) in bone marrow organoids. Scale bar: 50 µm.

Supplementary Fig. 6: Direct regulation of S100A8 by IRF8 restrains hypoxia-associated inflammatory niche remodeling.
(A) Volcano plots of selected, differentially expressed, fibrosis-associated genes in multipotent (n = 8,187 total genes) and inflammatory CAR cells (n = 7,514 total genes) and OLCs (n = 7,718 total genes), comparing *Irf8*$^{d/d}$ vs. *Irf8*$^{+/+}$ bone marrow chimeras and showing significant overlap with a reference myelofibrosis dataset. Fisher's exact test demonstrated significant enrichment with fibrotic MSC-1 for multipotent CAR cells (24 overlapping genes, odds ratio = 27.68 and p-value = $9{,}28 \times 10^{-23}$), inflammatory CAR cells (17 overlapping genes, ratio = 15.51, p-value = 1.84×10^{-13}), cycling CAR cells (24 overlapping genes, odds ratio = 4.63 and p-value = 1.86×10^{-7}), and OLCs (31 overlapping genes, odds ratio = 11.82 and p-value = 2.24×10^{-17}). Sigificant enrichment with MSC-2 was also observed across these stromal subsets, although with lower overlap and effect size compared with fibrotic MSC-1. **(B)** Heatmap of extracellular matrix-related pathways across selected cell populations, comparing *Irf8*$^{d/d}$ vs. *Irf8*$^{+/+}$ bone marrow chimeras. **(C)** Ridge plots of *Hif-1a*, *S100a8* and *S100a9* expression in CAR cell subsets and OLCs. **(D)** Overlap of transcription factor activity profiles across CAR cell subtypes and OLCs, showing enrichment of hypoxia-associated factors and

increased Hif1α–Arnt activity in *Irf8*$^{d/d}$ stromal populations. **(E)** Intracellular CrossTalkR analysis of cycling CAR cells. **(F)** Cell-cell interaction analysis comparing *Irf8*$^{d/d}$ with *Irf8*$^{+/+}$ chimeras. **(G, H)** Intracellular S100A8 staining in bone marrow **(G)** and spleen **(H)** by flow cytometry of *Irf8*$^{+/+}$ and *Irf8*$^{d/d}$ mice. Dotted line represents background mean fluorescence intensity at a value of 600. **(I)** Representative CODEX microscopy images of Gli1 *Irf8*$^{d/d}$ and Gli1 *Irf8*$^{+/+}$ spleens showing deposition of inflammatory S100A8/9^{+} cells in the red pulp and disorganized white pulp structures. Scale bar: 100 µm.

Supplementary Fig. 7: St S100A8/A9 inflammatory niche remodeling promotes BRC–ABL-driven disease progression and fibrosis.

Panels (A-F) correspond to the transplanted mouse experiment shown in Figure 7A. **(A)** Peripheral blood counts in *Irf8*$^{d/d}$ vs. *Irf8*$^{+/+}$ recipients transplanted with pMIG- or BCR-ABL-transduced c-Kit enriched bone marrow cells, revealing normal counts in controls but marked leukocytosis in BCR-ABL-transplanted mice. **(B)** Frequencies of peripheral blood immune cell populations determined by flow cytometry. **(C,D)** Frequencies of hematopoietic stem and progenitor cells in bone marrow **(C)** and spleen **(D)** determined by flow cytometry. **(E,F)** Frequencies of bone marrow **(E)** and spleen **(F)** immune cell populations determined by flow cytometry. **(G)** Reticulin staining of bone marrow biopsies in a CML patient cohort: grades 0 and 1 (N = 15), grade 2 (N = 4), stratified by fibrosis severity. and used to correlate S100A8/9 staining intensity and fibrosis grade in the same cohort **(H)**.

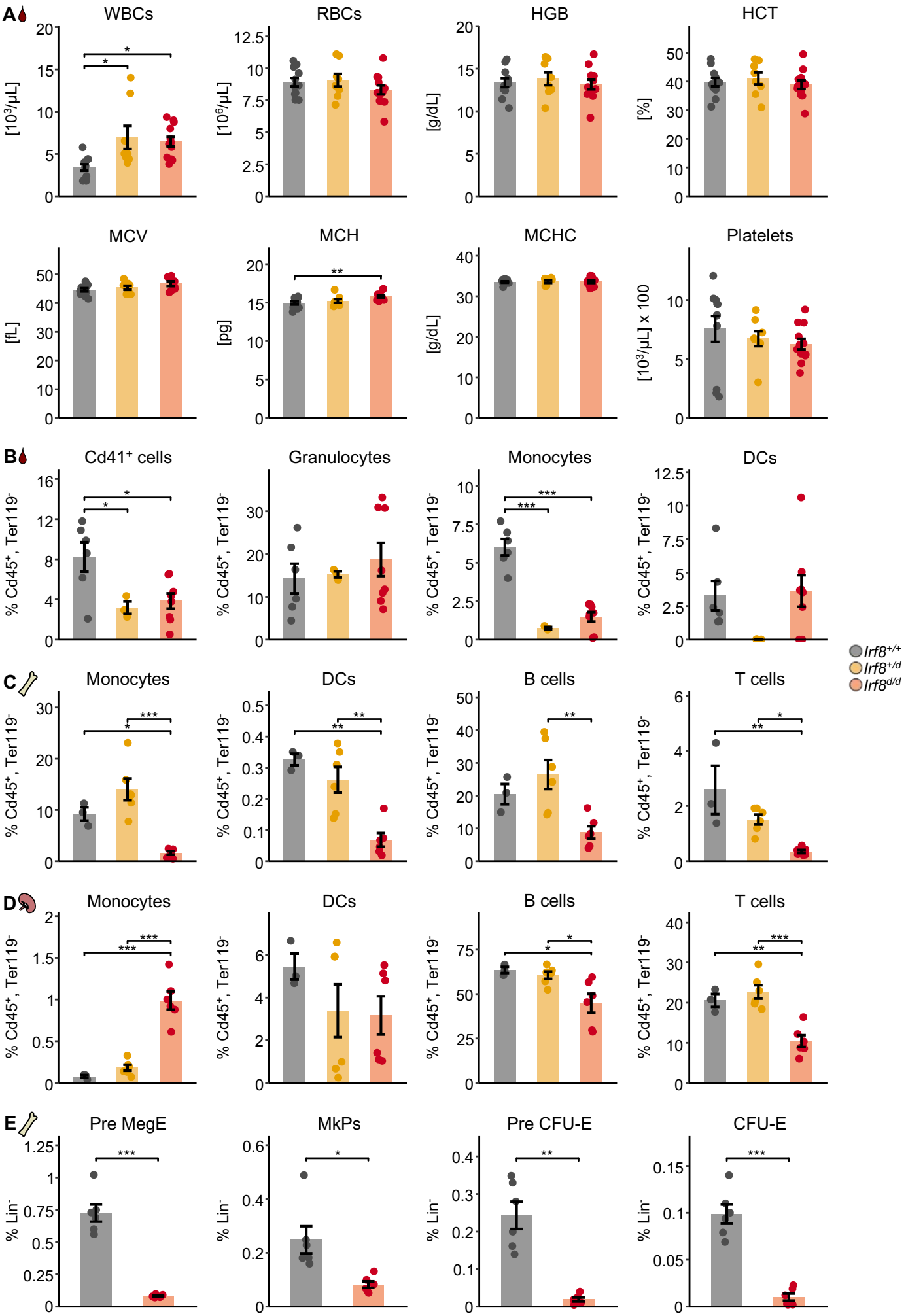

SUPPLEMENTARY FIGURE 1

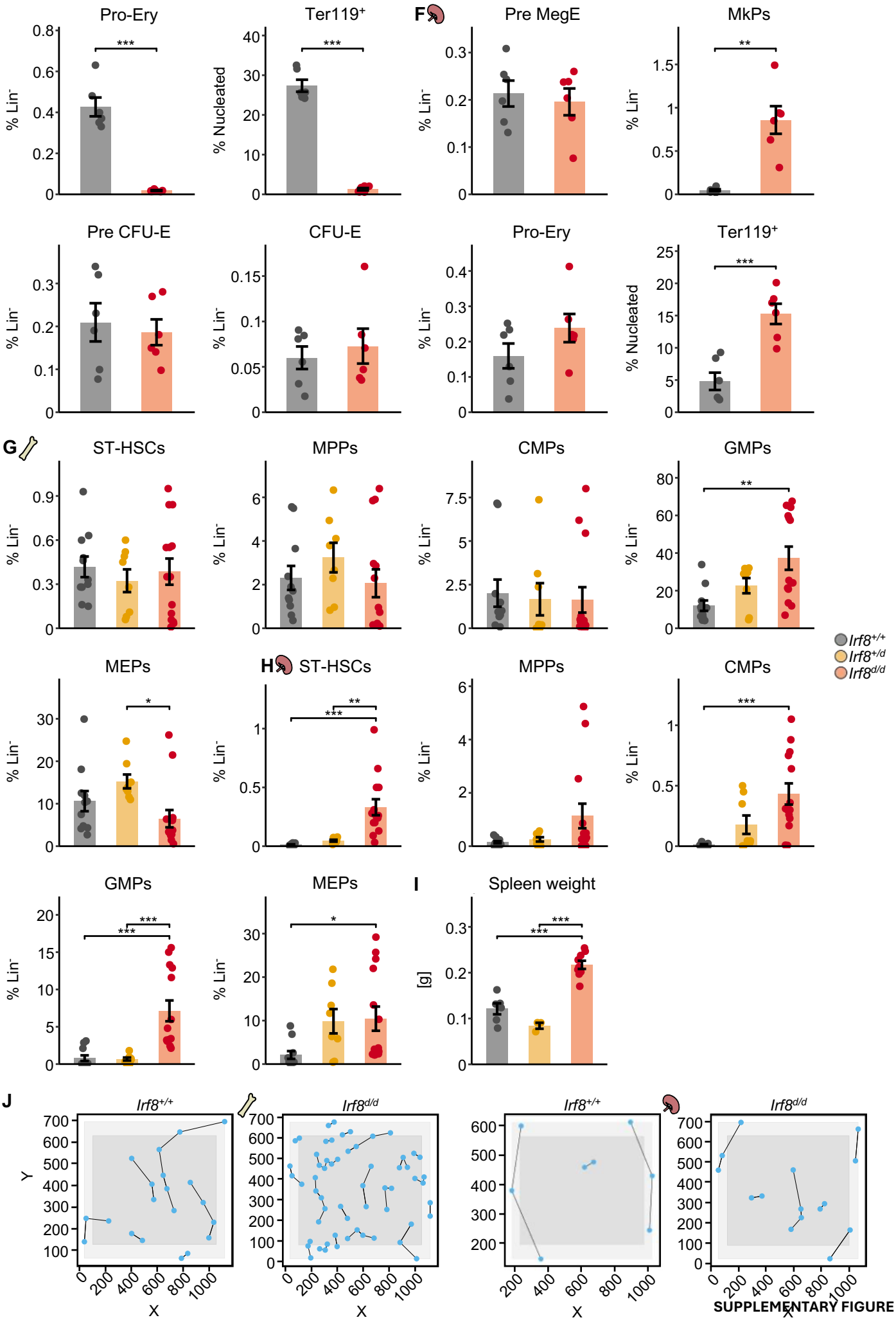

SUPPLEMENTARY FIGURE 1

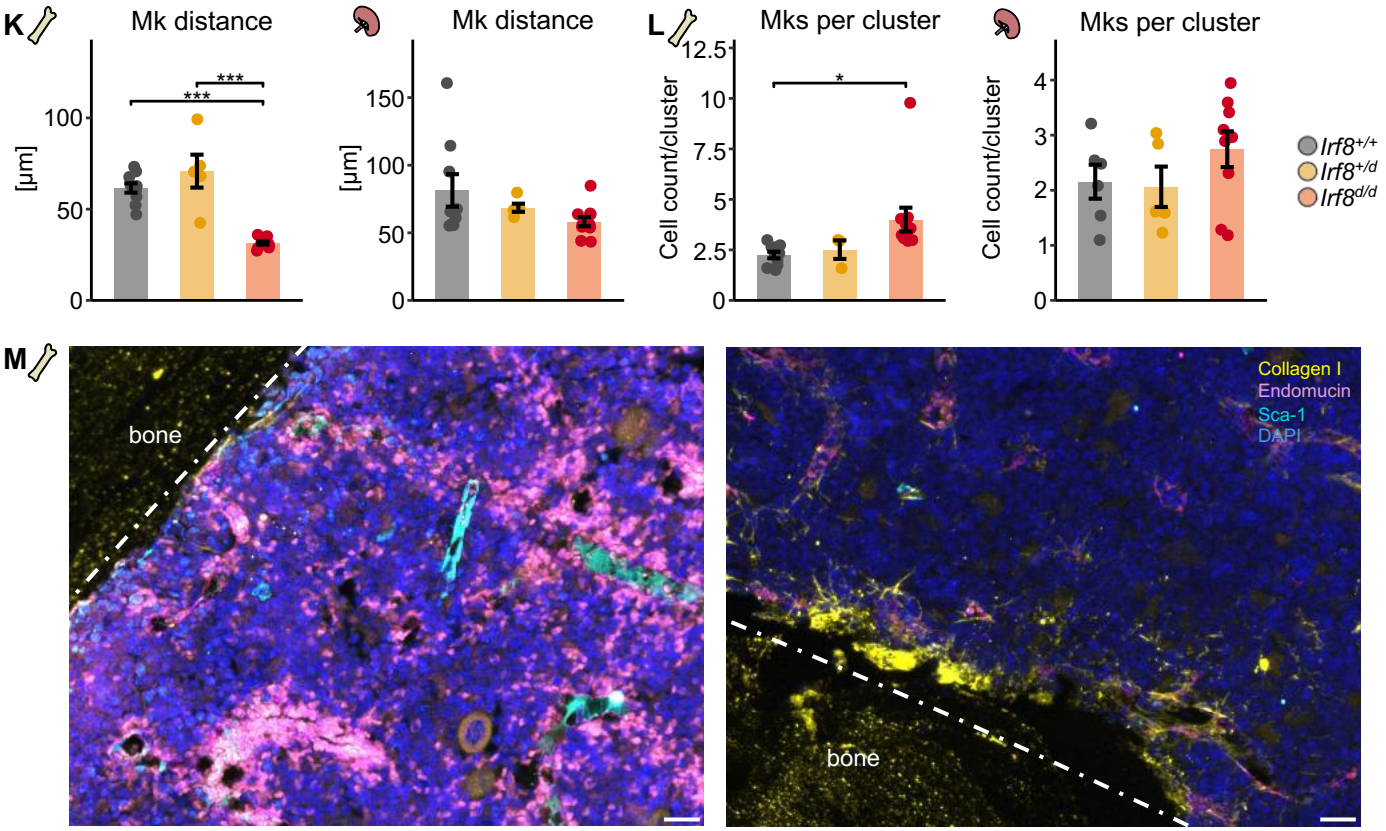

SUPPLEMENTARY FIGURE 1

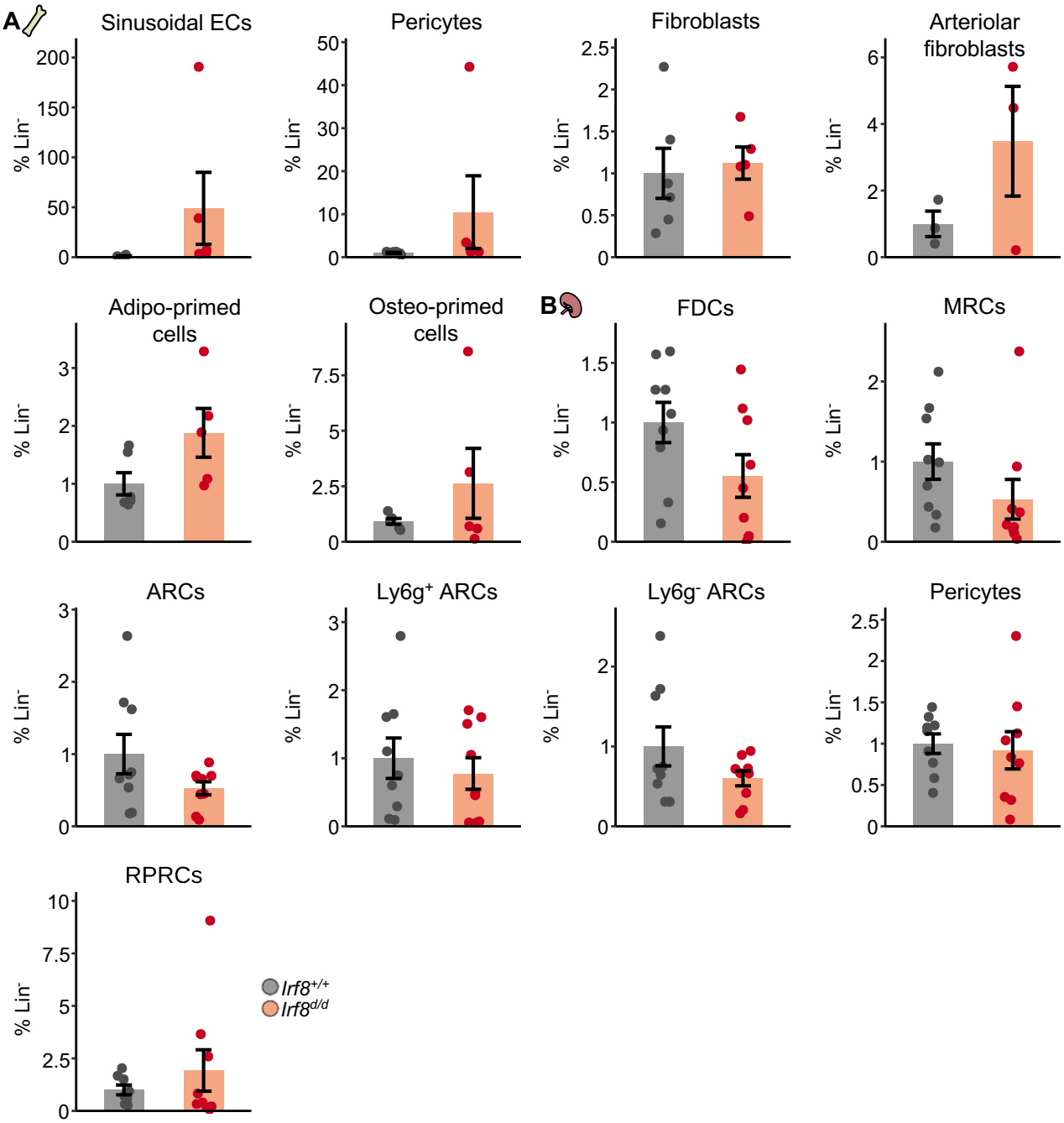

SUPPLEMENTARY FIGURE 2

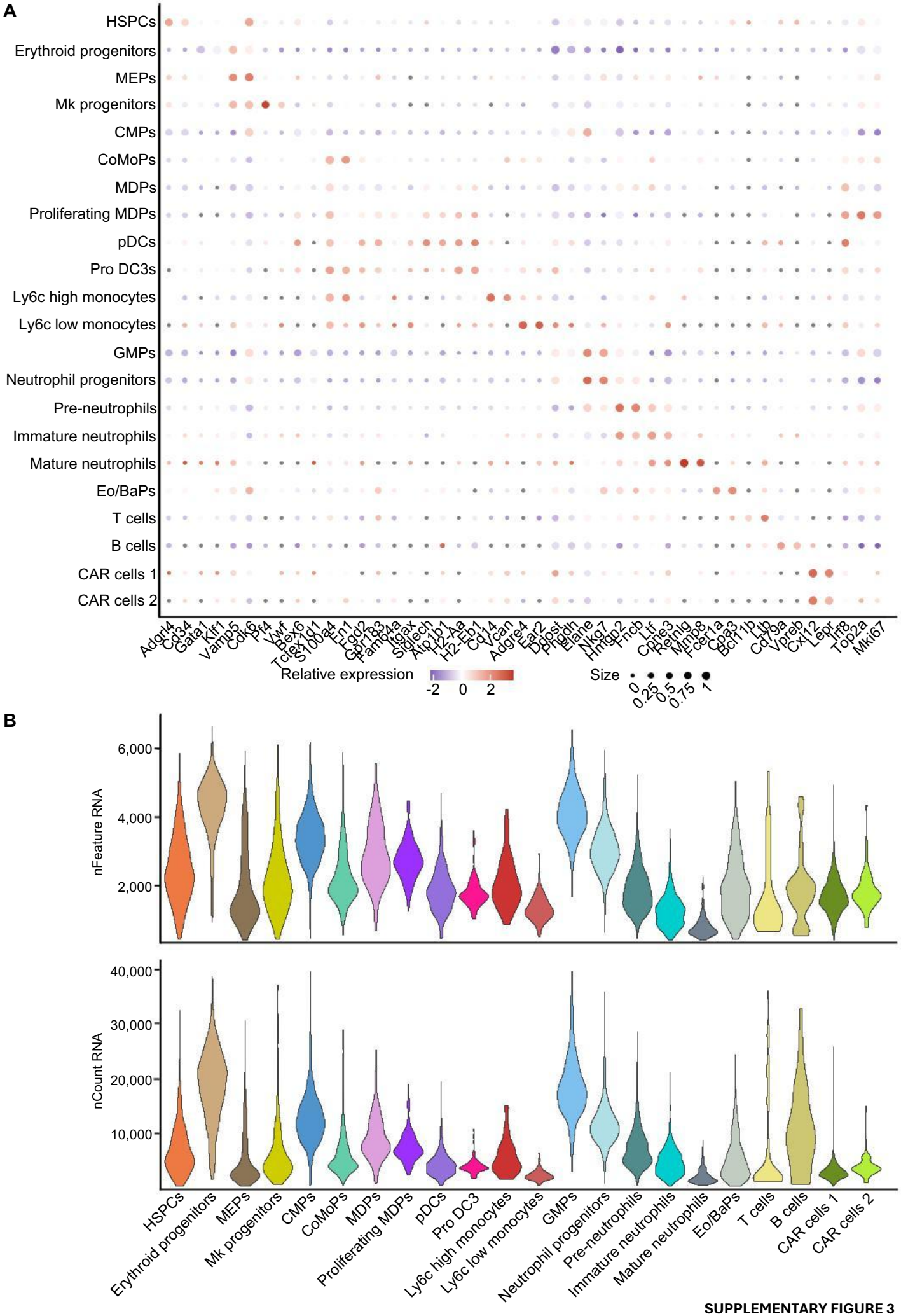

SUPPLEMENTARY FIGURE 3

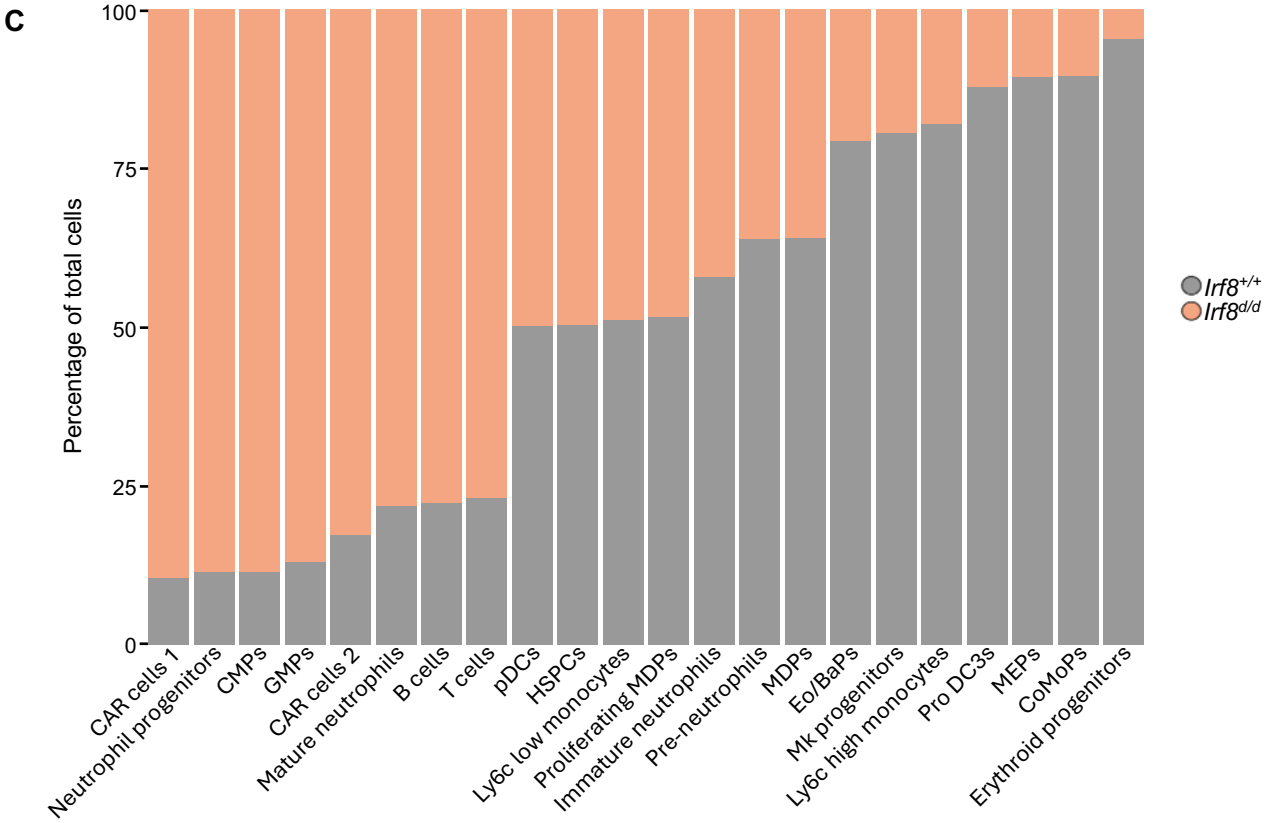

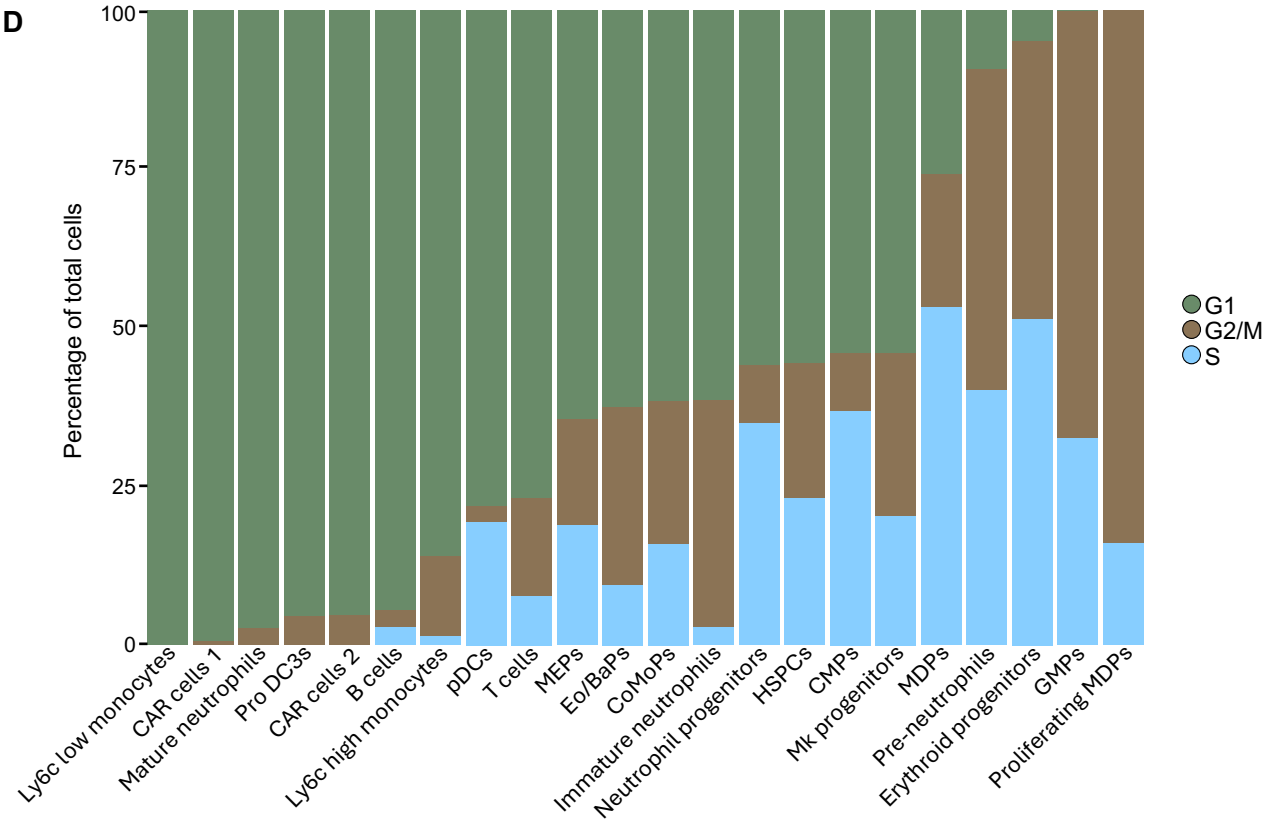

SUPPLEMENTARY FIGURE 3

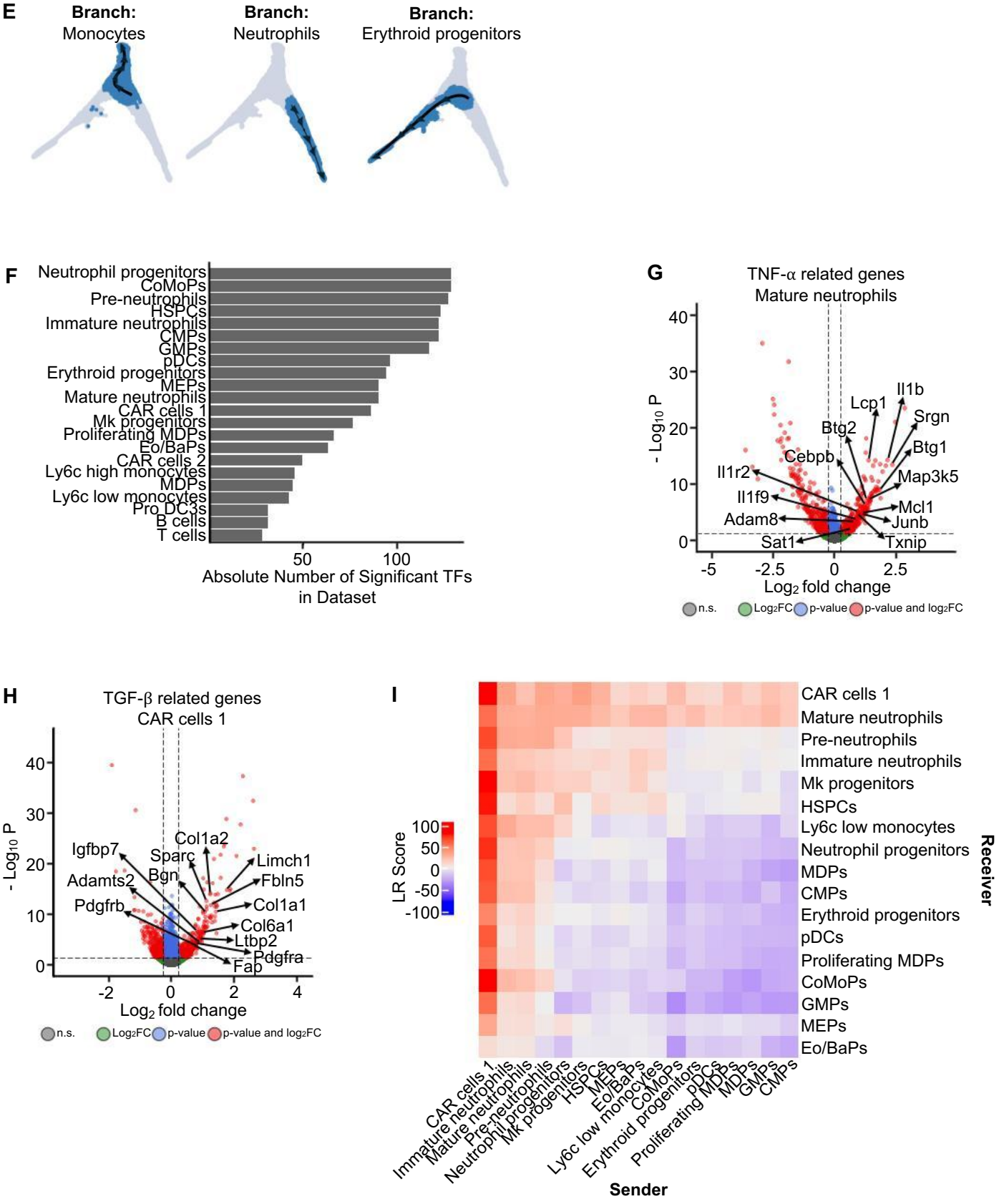

SUPPLEMENTARY FIGURE 3

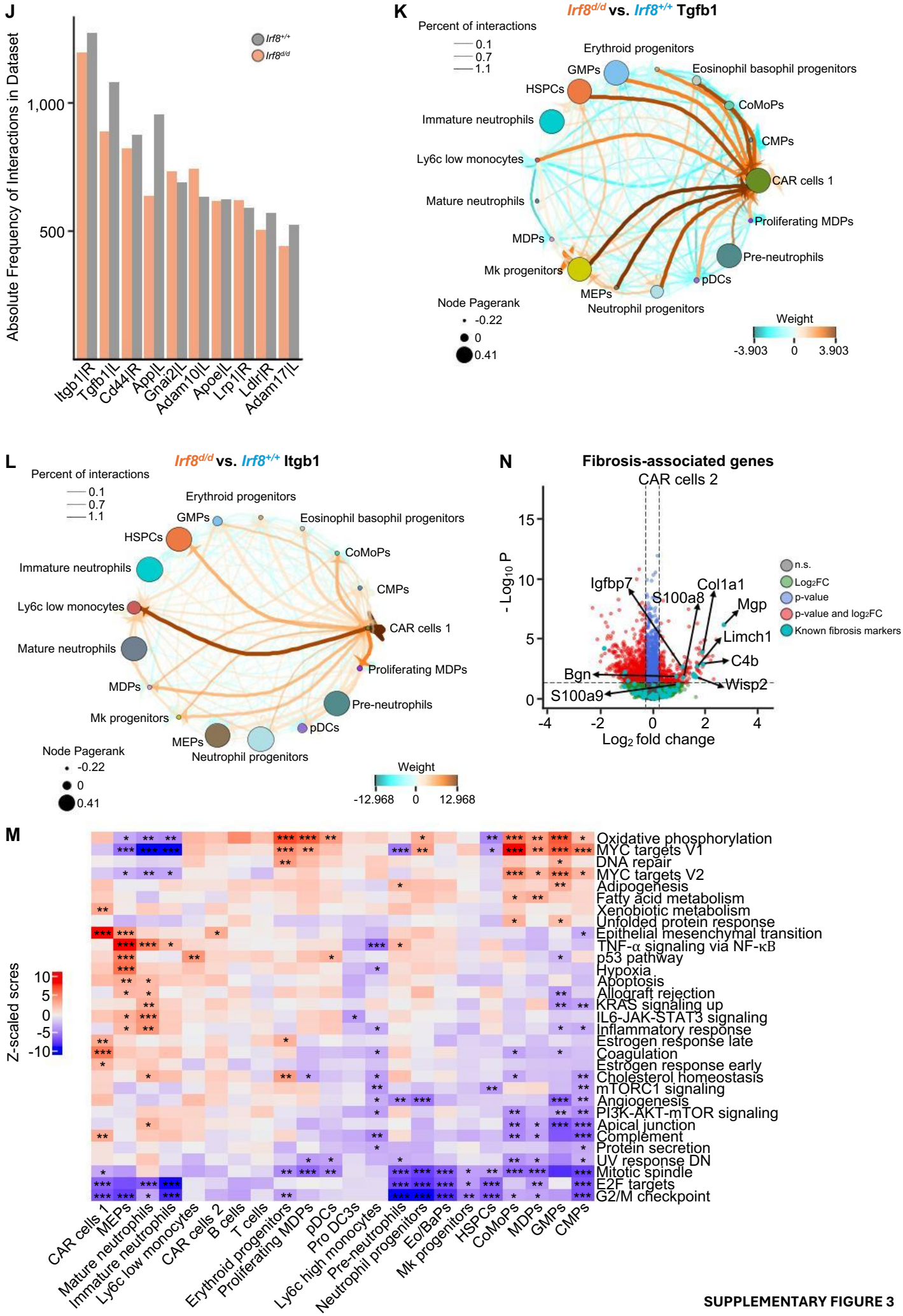

SUPPLEMENTARY FIGURE 3

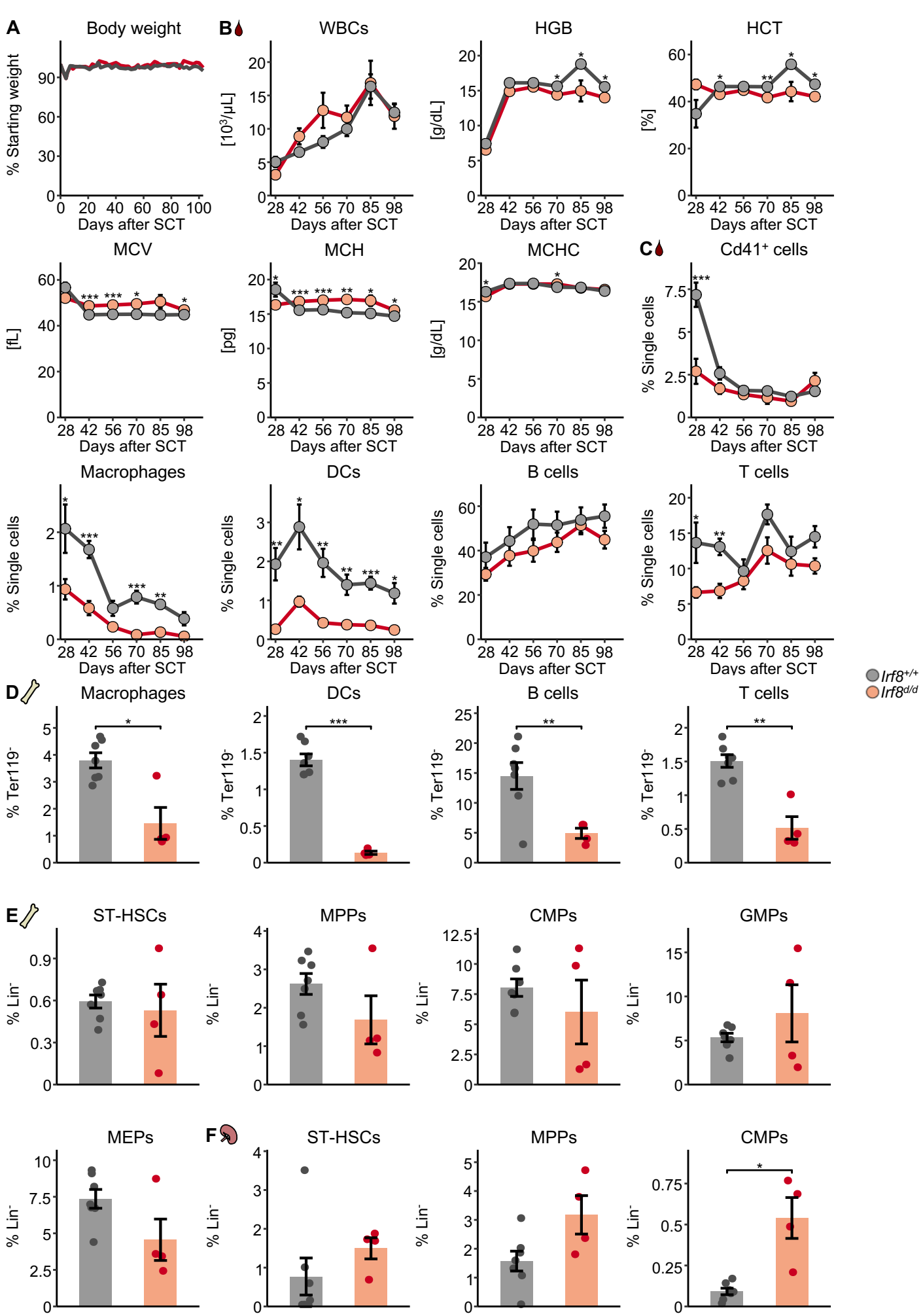

SUPPLEMENTARY FIGURE 4

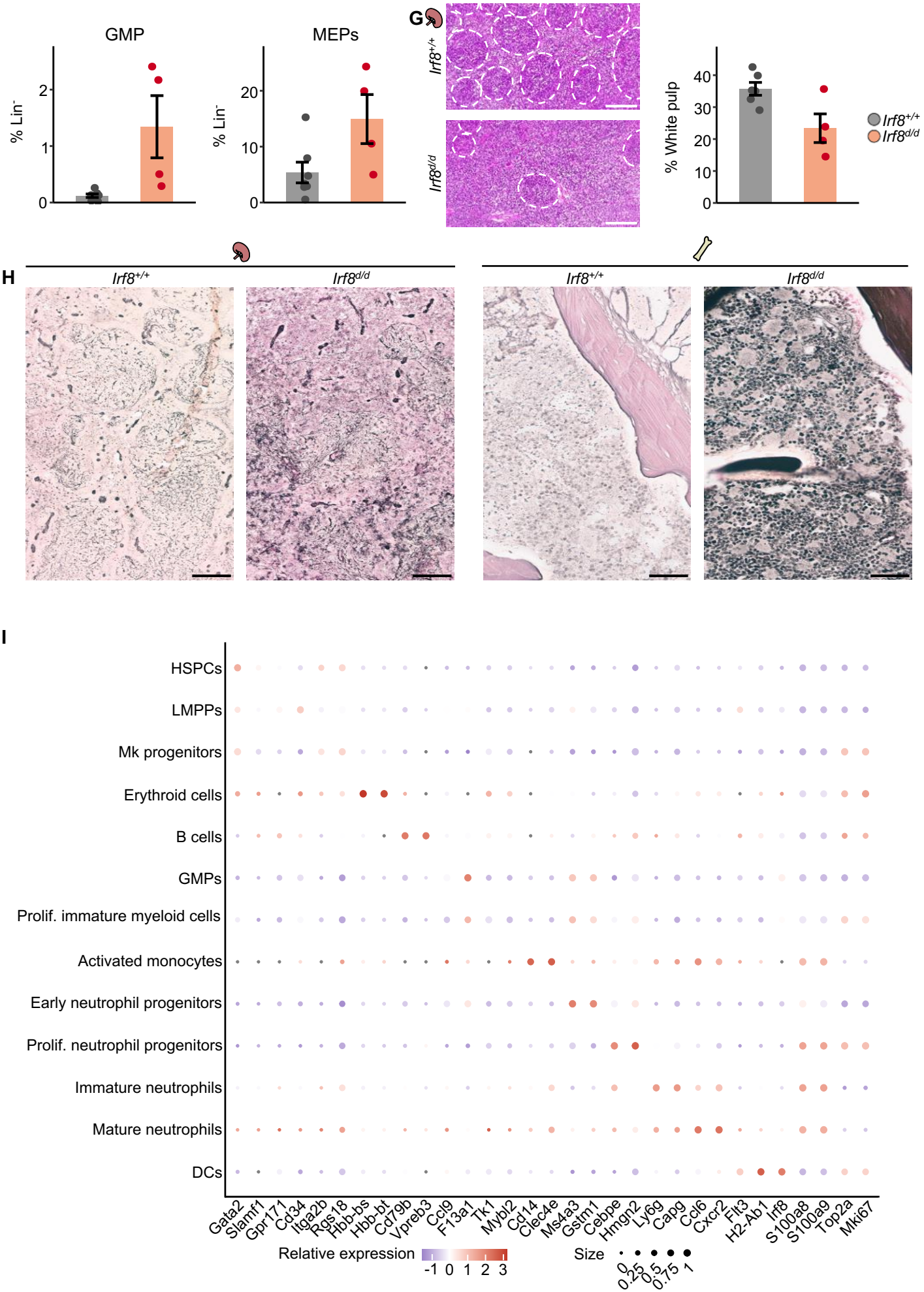

SUPPLEMENTARY FIGURE 4

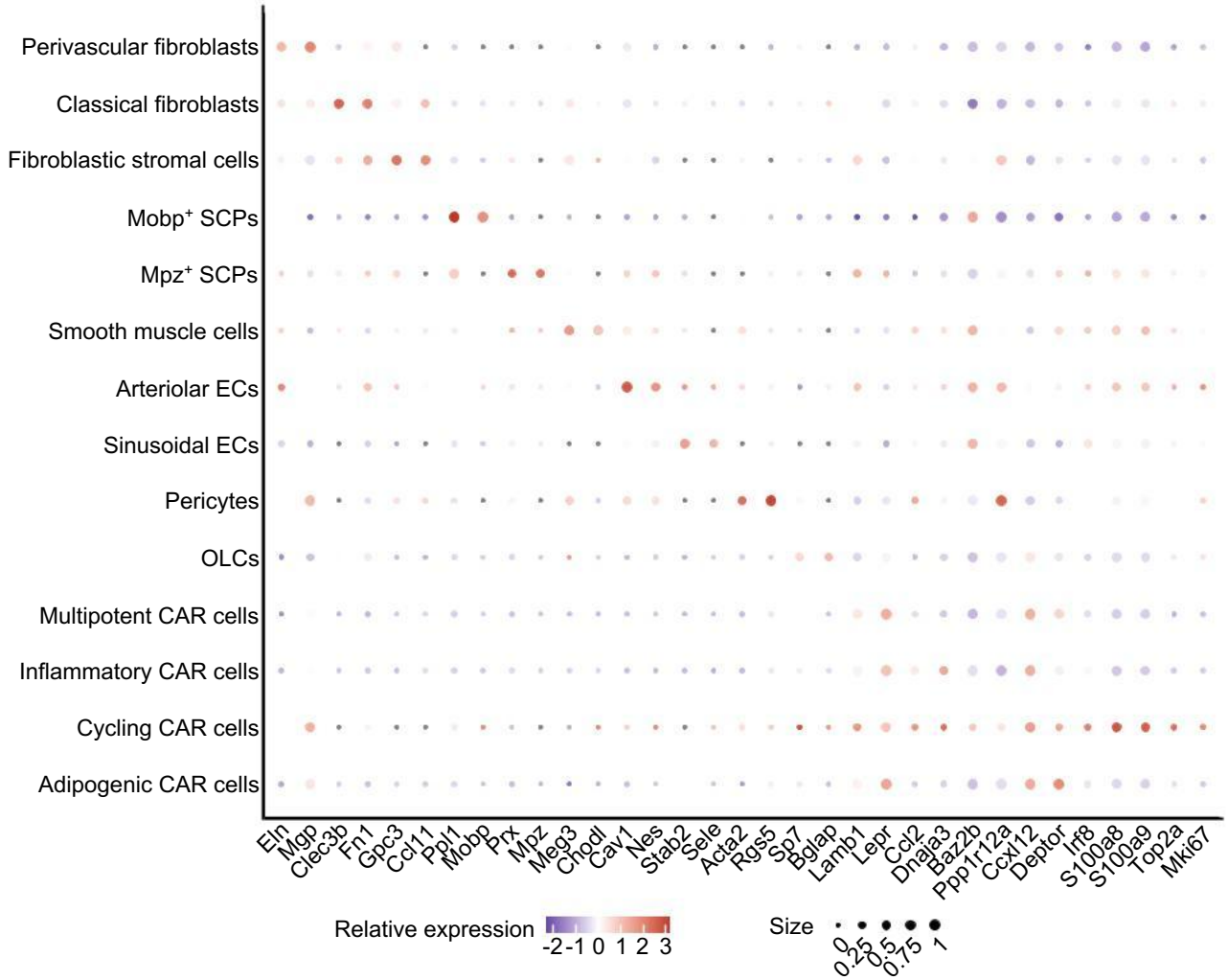

J

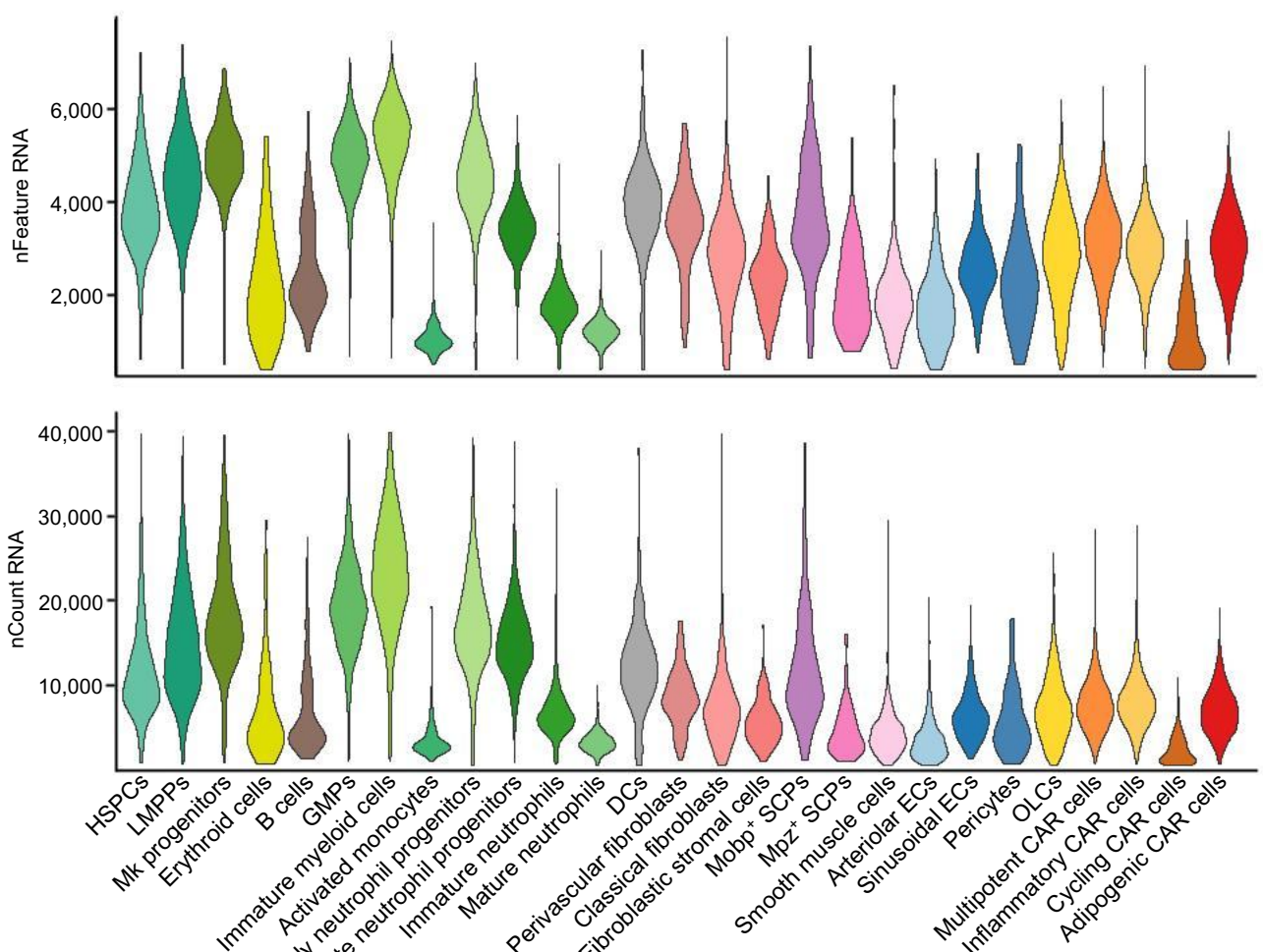

SUPPLEMENTARY FIGURE 4

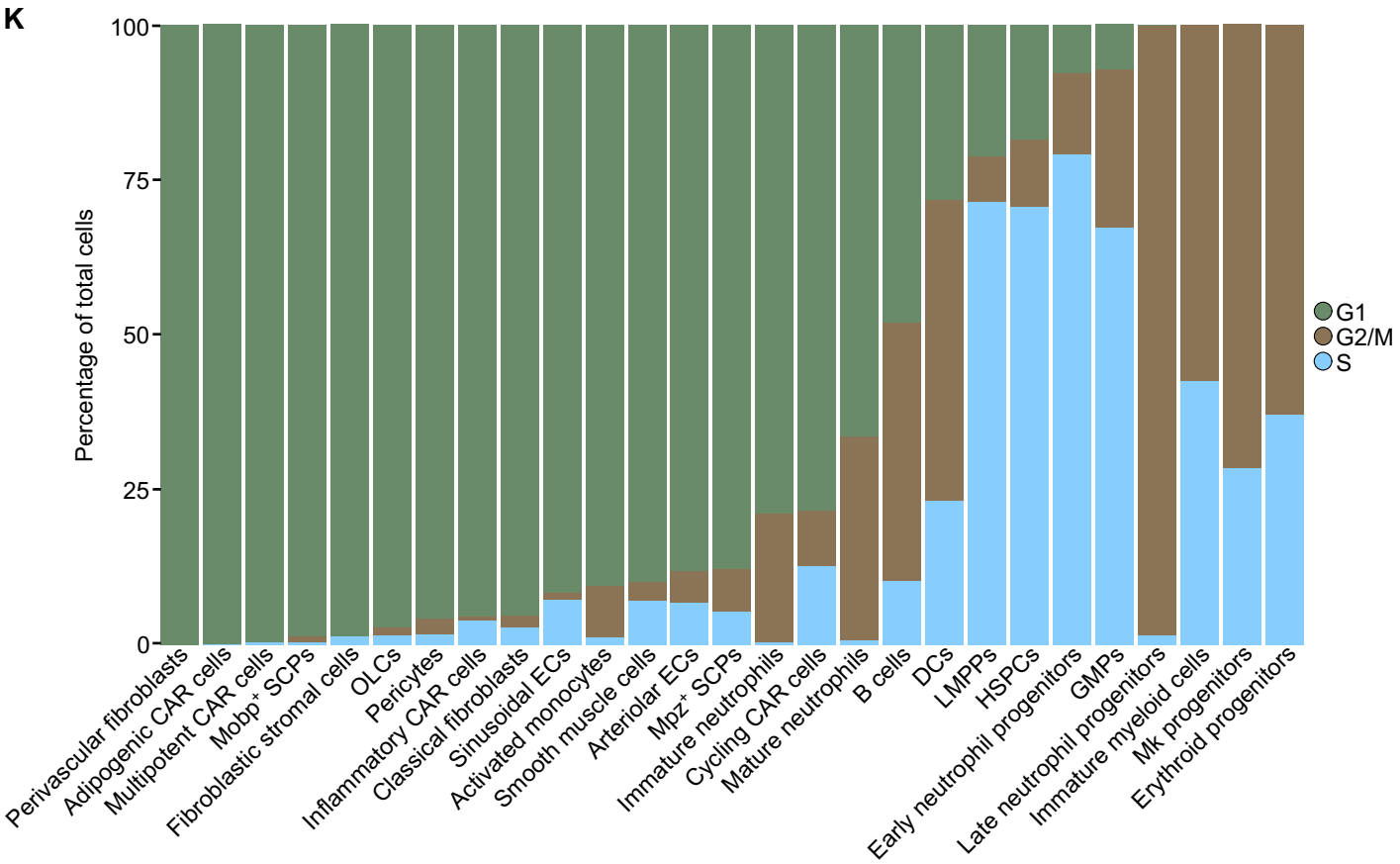

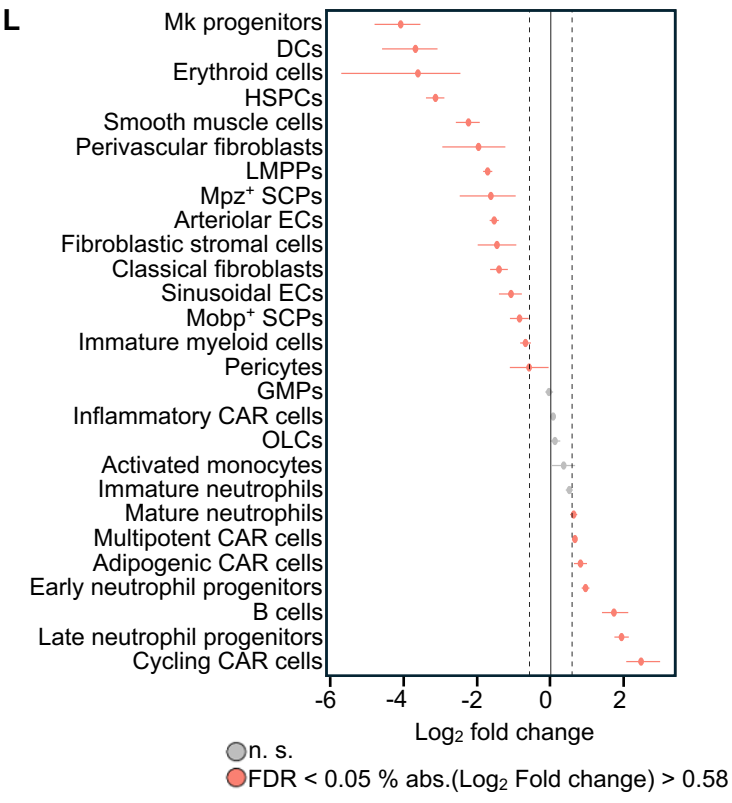

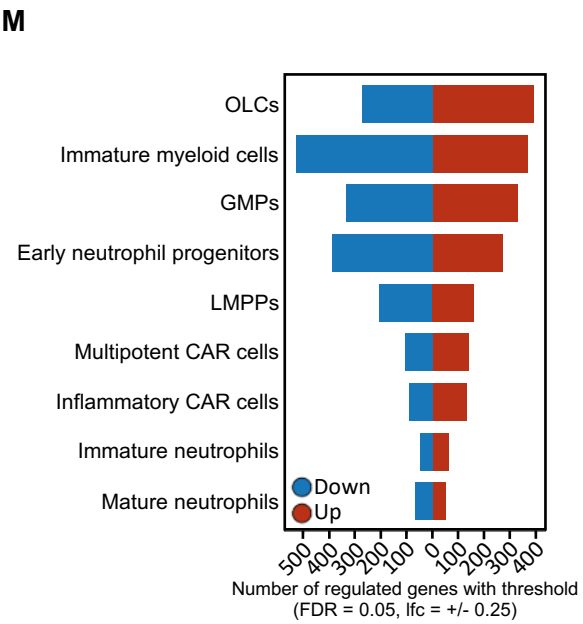

SUPPLEMENTARY FIGURE 4

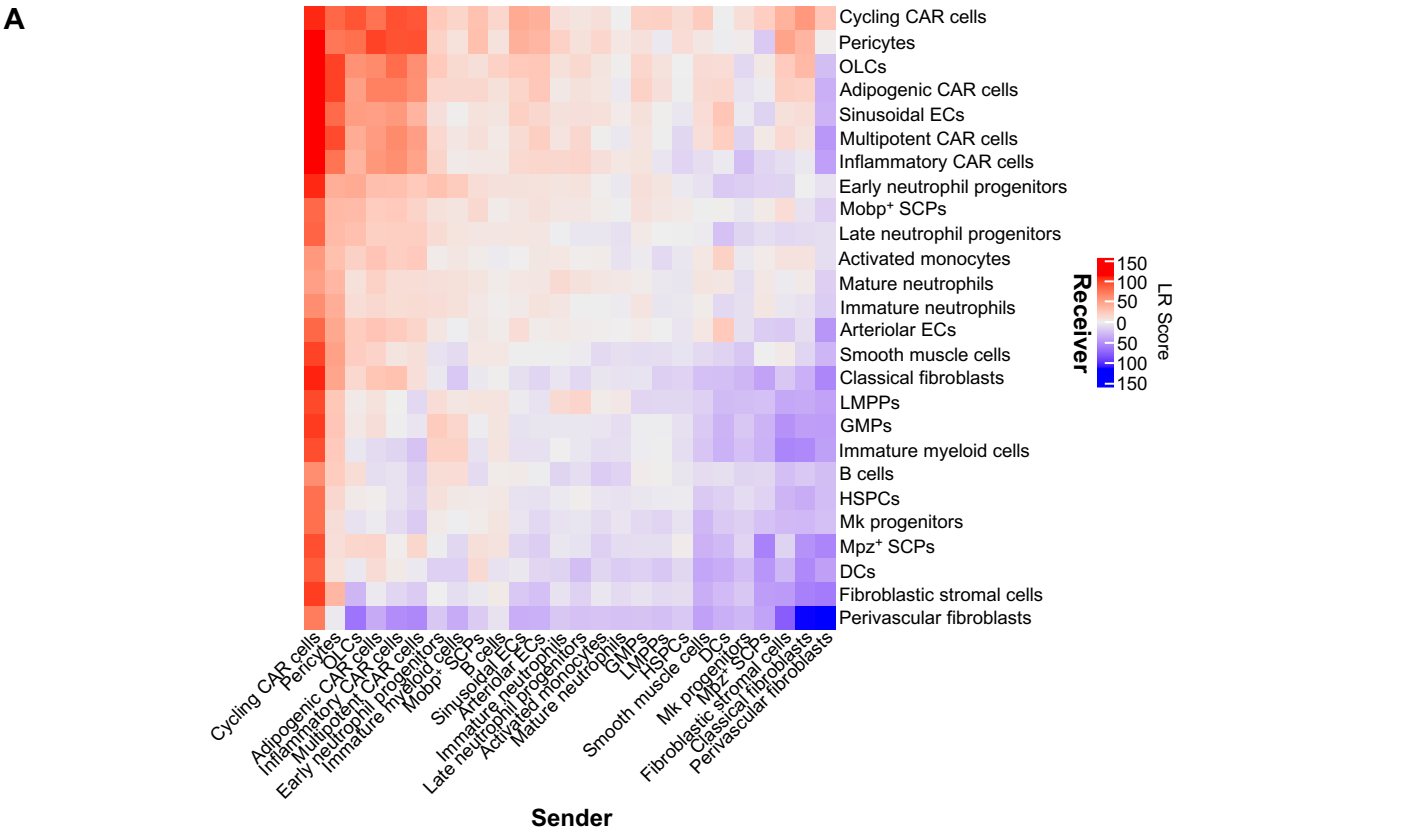
A
Cycling CAR cells
Pericytes
OLCs
Adipogenic CAR cells
Sinusoidal ECs
Multipotent CAR cells
Inflammatory CAR cells
Early neutrophil progenitors
Mobp+ SCPs
Late neutrophil progenitors
Activated monocytes
Mature neutrophils
Immature neutrophils
Arteriolar ECs
Smooth muscle cells
Classical fibroblasts
LMPPs
GMPs
Immature myeloid cells
B cells
HSPCs
Mk progenitors
Mpz+ SCPs
DCs
Fibroblastic stromal cells
Perivascular fibroblasts
Receiver
LR Score
150
100
50
0
50
100
150
Sender

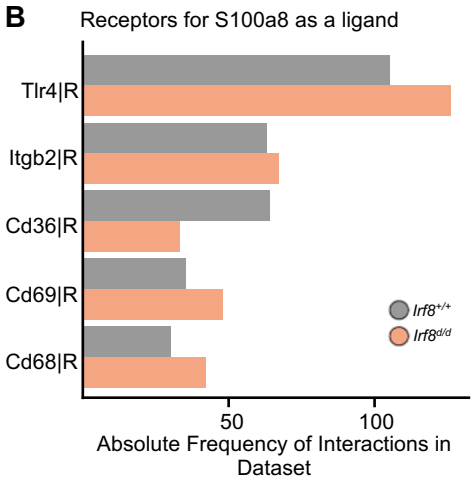
B
Receptors for S100a8 as a ligand
Tlr4|R
Itgb2|R
Cd36|R
Cd69|R
Cd68|R
Irf8+/+
Irf8d/d
50
100
Absolute Frequency of Interactions in Dataset

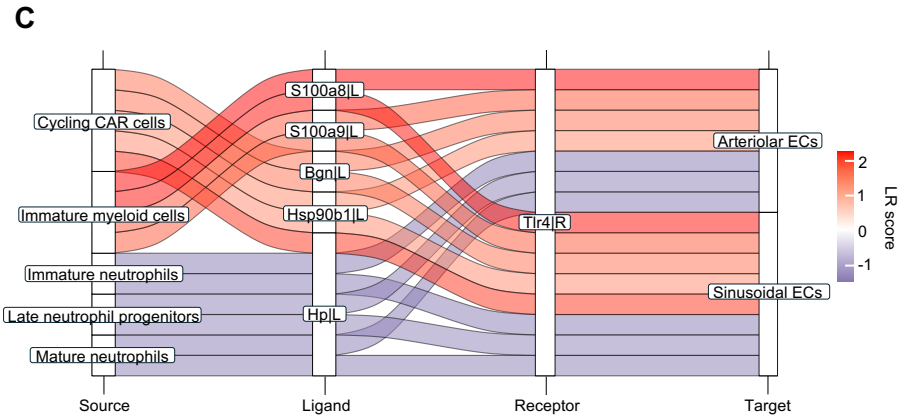
C
Cycling CAR cells
Immature myeloid cells
Immature neutrophils
Late neutrophil progenitors
Mature neutrophils
S100a8|L
S100a9|L
Bgn|L
Hsp90b1|L
Hp|L
Tlr4|R
Arteriolar ECs
Sinusoidal ECs
LR score
2
1
0
-1
Source
Ligand
Receptor
Target

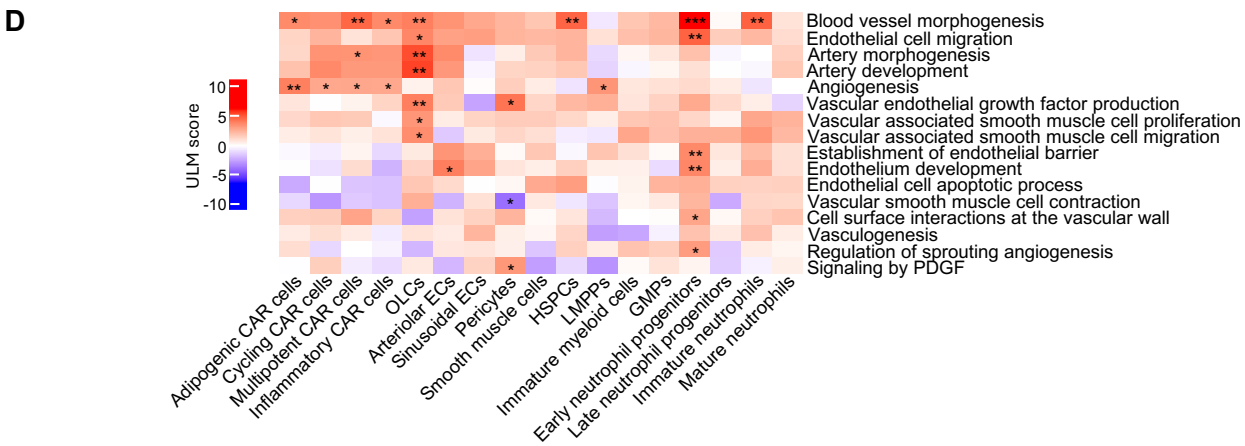
D
ULM score
10
5
0
-5
-10
Blood vessel morphogenesis
Endothelial cell migration
Artery morphogenesis
Artery development
Angiogenesis
Vascular endothelial growth factor production
Vascular associated smooth muscle cell proliferation
Vascular associated smooth muscle cell migration
Establishment of endothelial barrier
Endothelium development
Endothelial cell apoptotic process
Vascular smooth muscle cell contraction
Cell surface interactions at the vascular wall
Vasculogenesis
Regulation of sprouting angiogenesis
Signaling by PDGF
Adipogenic CAR cells
Cycling CAR cells
Multipotent CAR cells
Inflammatory CAR cells
OLCs
Arteriolar ECs
Sinusoidal ECs
Pericytes
Smooth muscle cells
HSPCs
LMPPs
Immature myeloid cells
GMPs
Early neutrophil progenitors
Late neutrophil progenitors
Immature neutrophils
Mature neutrophils

E

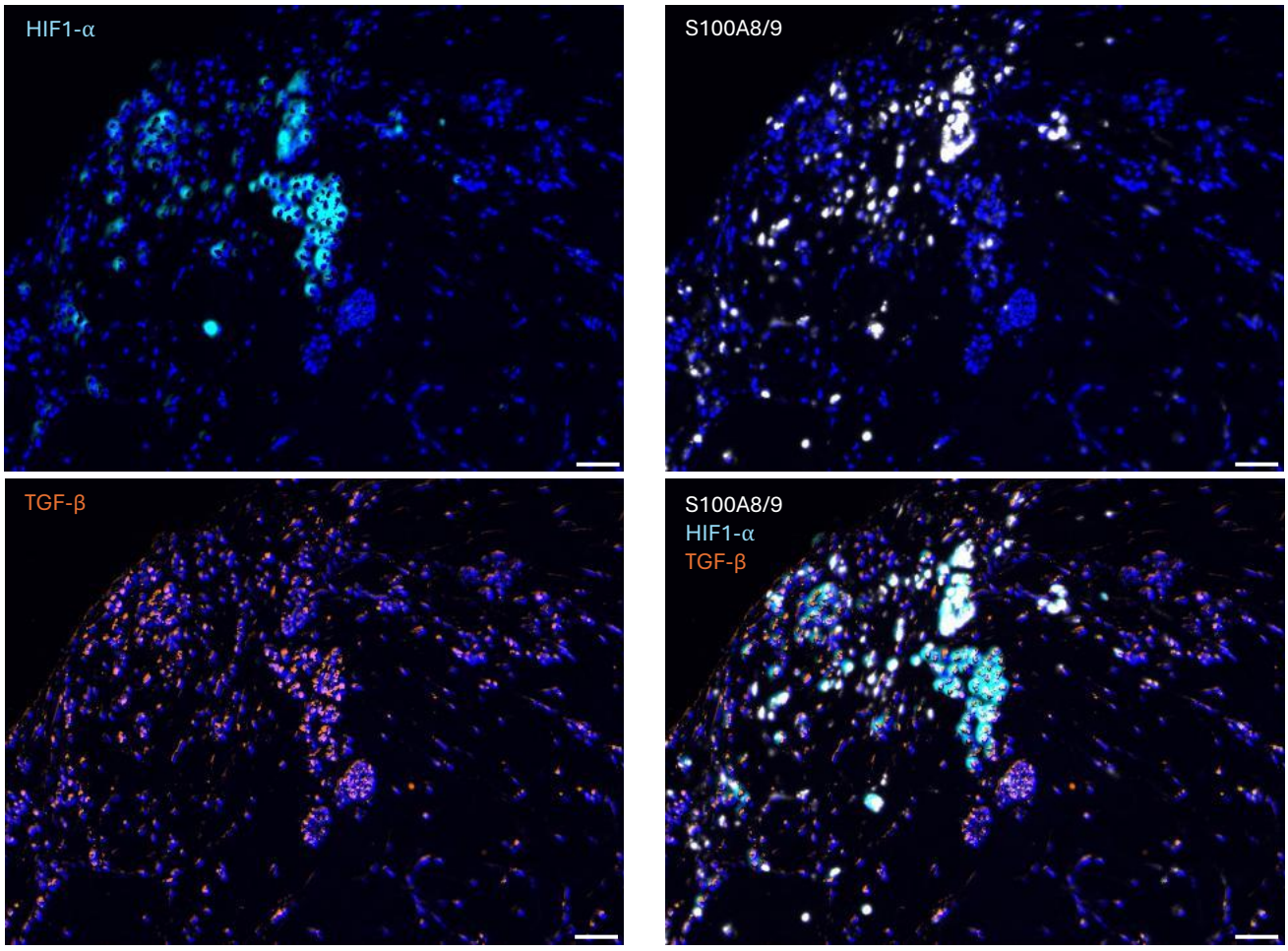

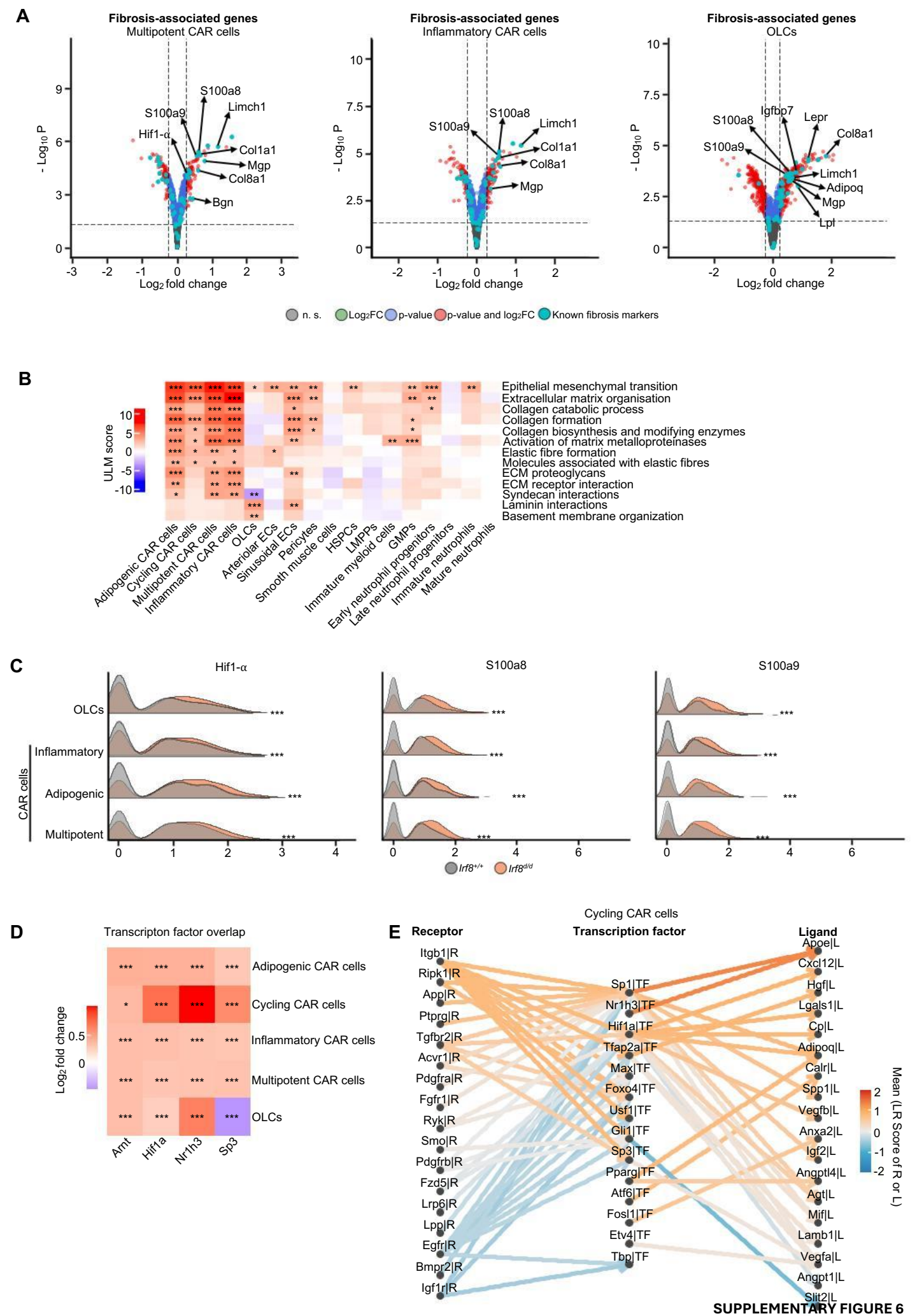

SUPPLEMENTARY FIGURE 6

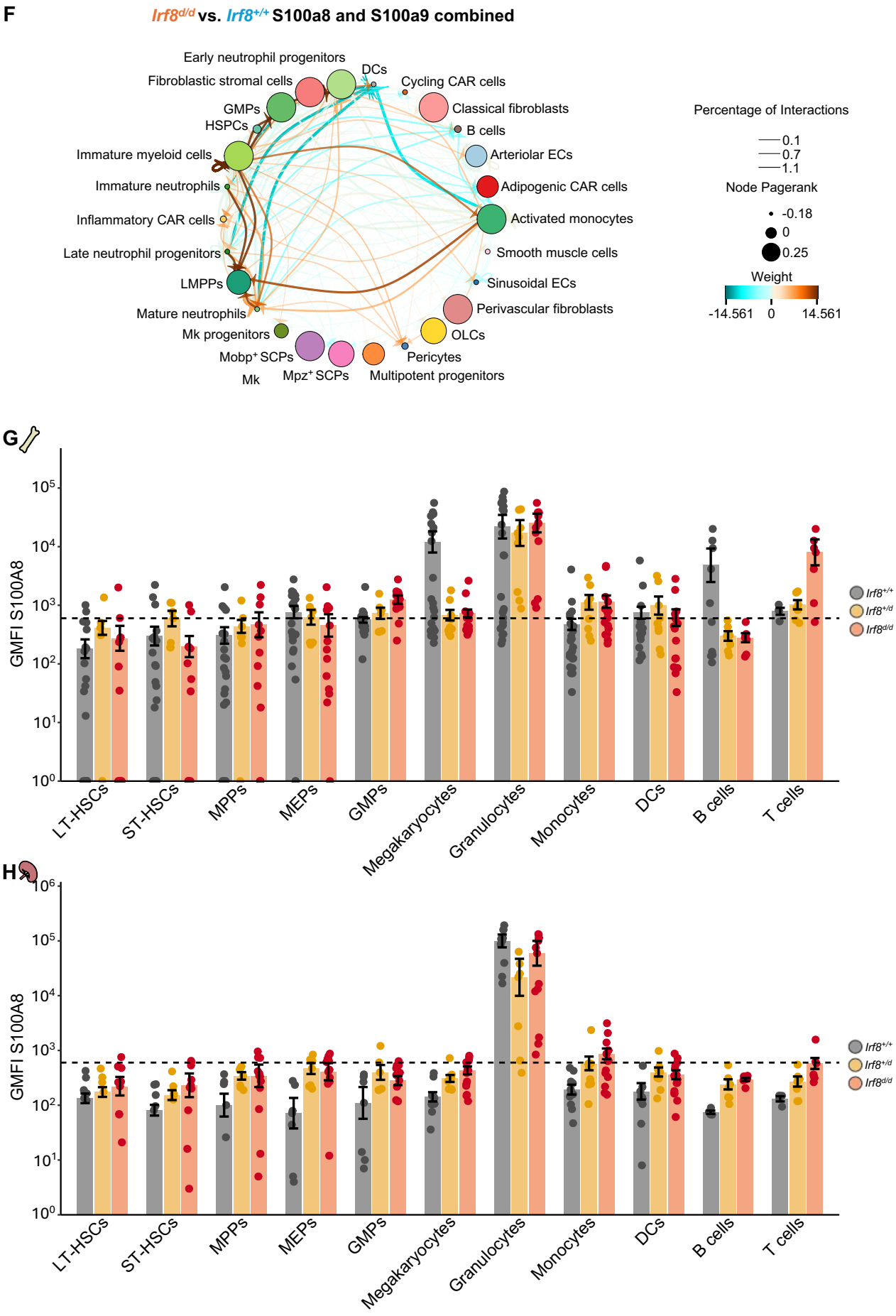

SUPPLEMENTARY FIGURE 6

I

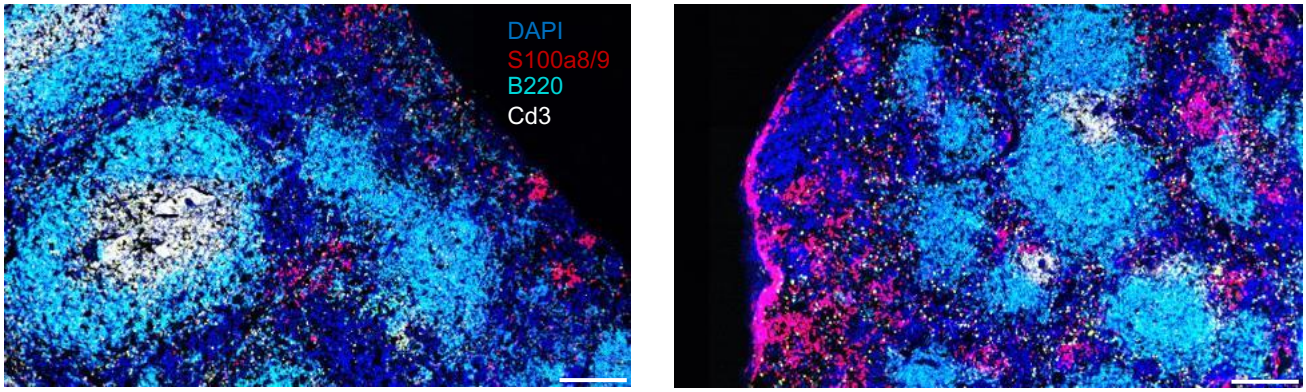

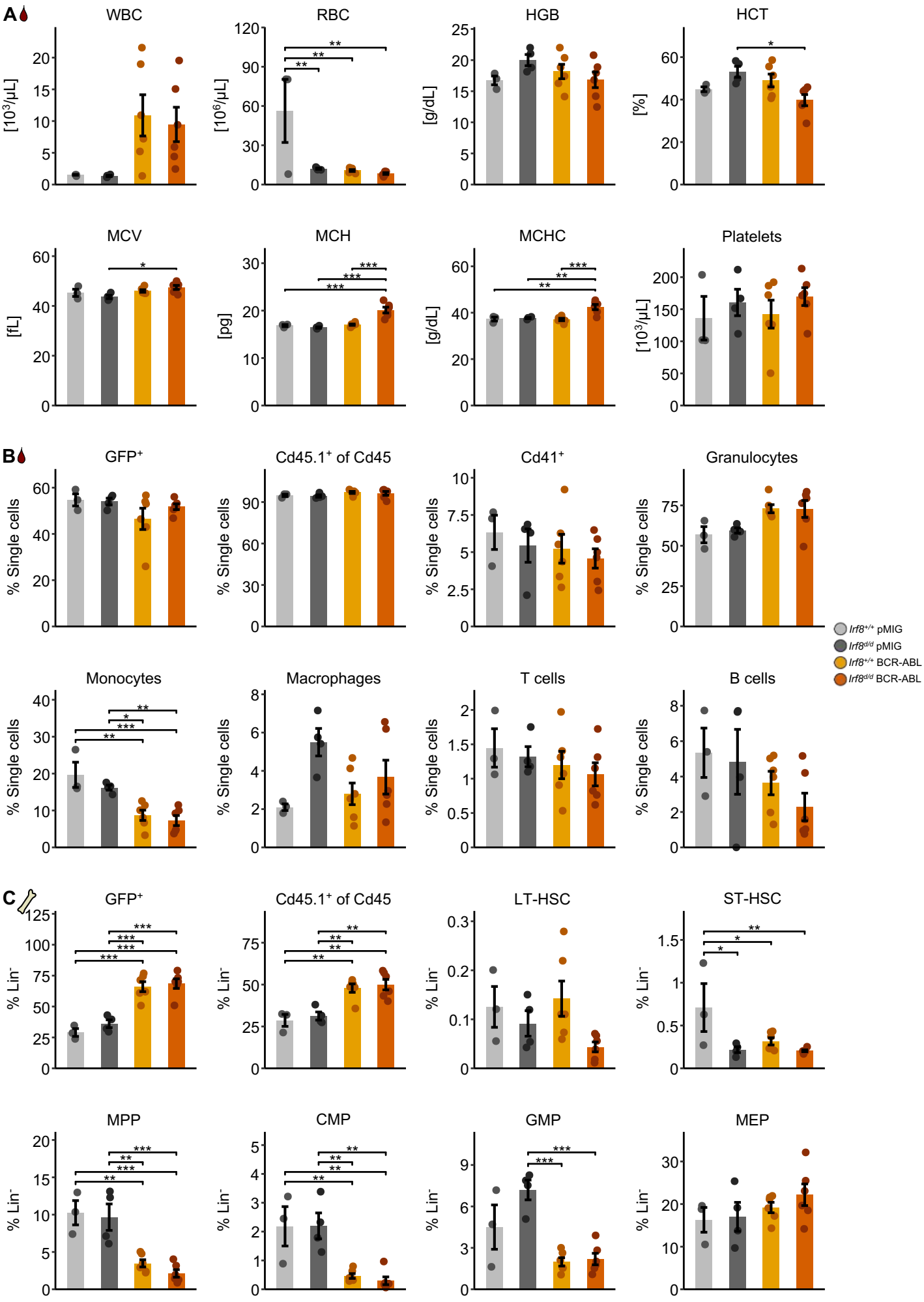

SUPPLEMENTARY FIGURE 7

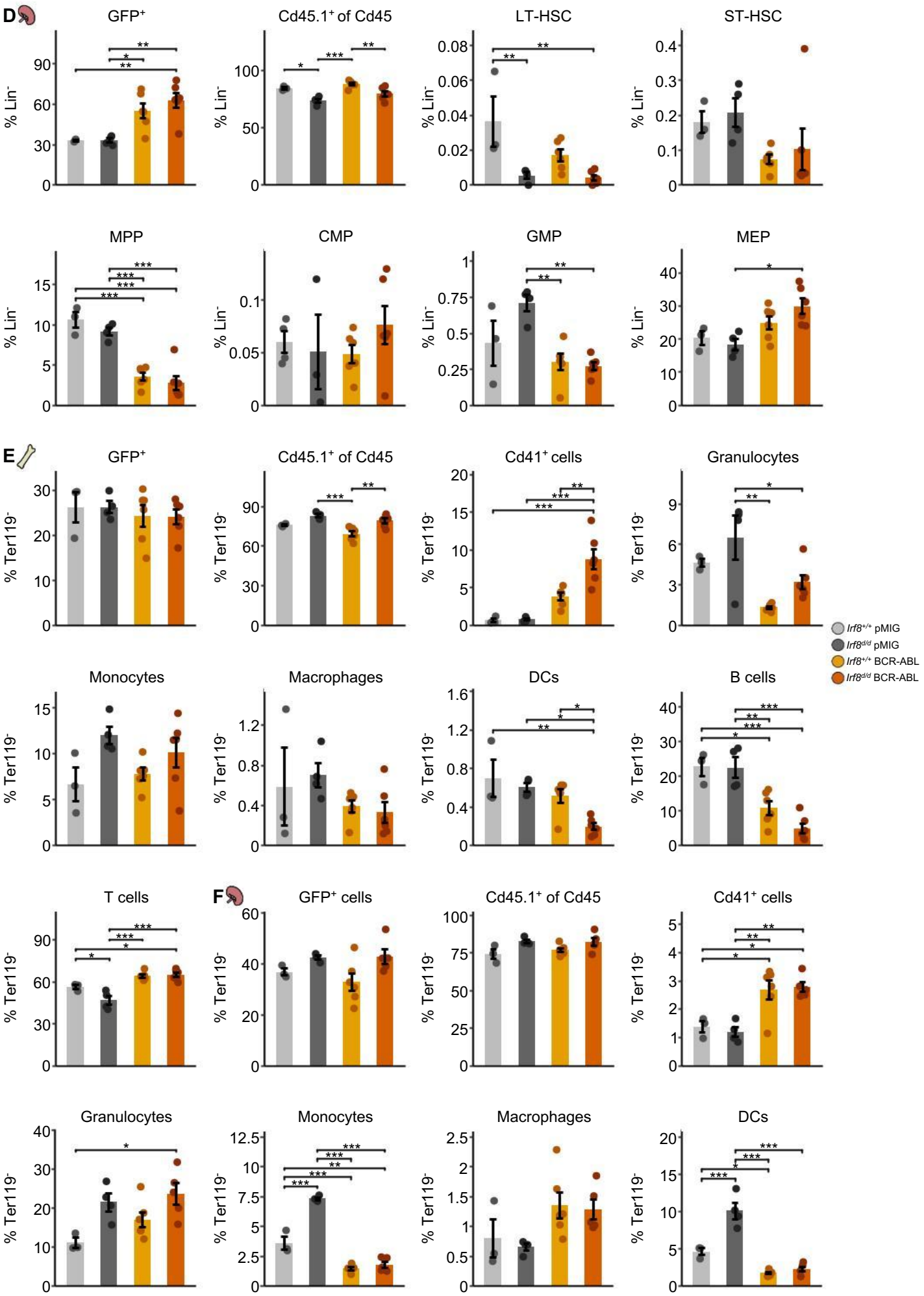

SUPPLEMENTARY FIGURE 7

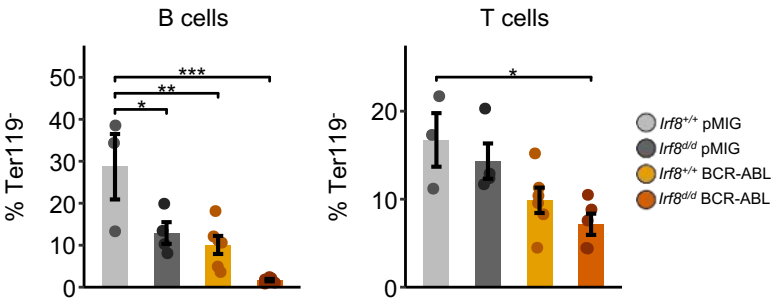
B cells
T cells
% Ter119-
50
40
30
20
10
0
***
**
*
*
Irf8+/+ pMIG
Irf8d/d pMIG
Irf8+/+ BCR-ABL
Irf8d/d BCR-ABL

G

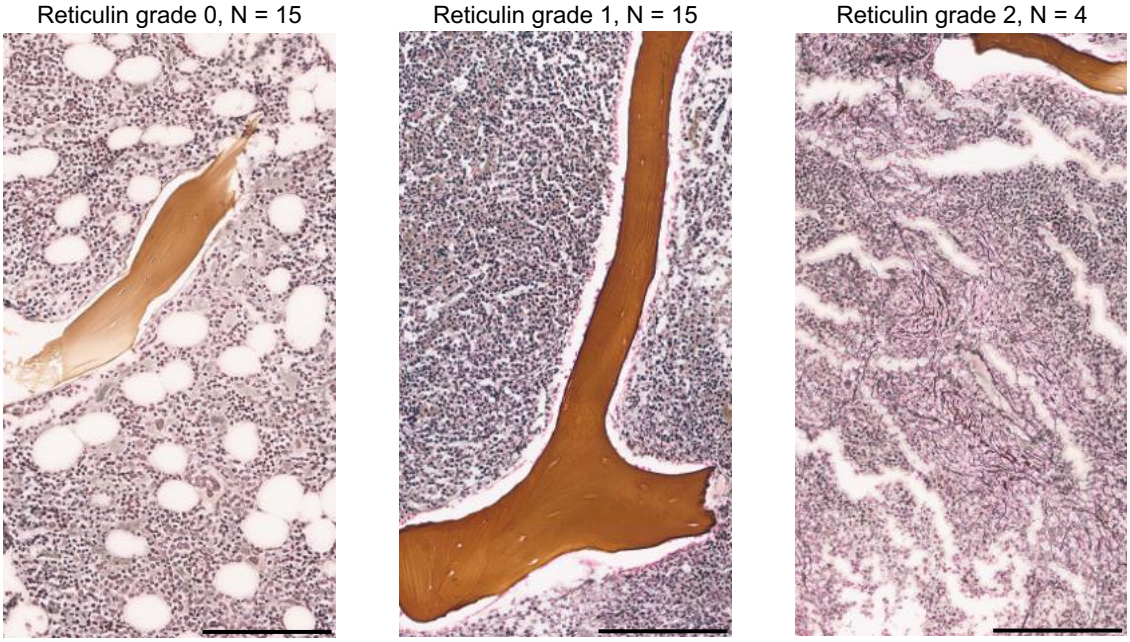
Reticulin grade 0, N = 15
Reticulin grade 1, N = 15
Reticulin grade 2, N = 4